Stratigraphy of the Archean western Superior Province from P- and S-wave receiver functions: further evidence for tectonic accretion?

D.A. Angus, J- M. Kendall, D.C. Wilson, D.J. White, S. Sol, C.J. Thomson

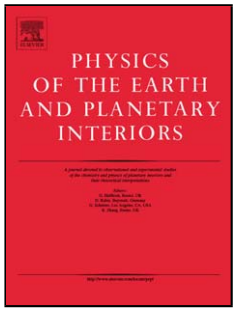

Title: Stratigraphy of the Archean western Superior Province from P– and S–wave receiver functions: further evidence for tectonic accretion?

Authors: D.A. Angus, J– M. Kendall, D.C. Wilson, D.J. White, S. Sol, C.J. Thomson

PII: S0031-9201(09)00197-6
DOI: doi:10.1016/j.pepi.2009.09.002
Reference: PEPI 5205

To appear in: *Physics of the Earth and Planetary Interiors*

Received date: 6-5-2007
Revised date: 12-8-2009
Accepted date: 10-9-2009

Please cite this article as: Angus, D.A., Kendall, J.M., Wilson, D.C., White, D.J., Sol, S., Thomson, C.J., Stratigraphy of the Archean western Superior Province from P– and S–wave receiver functions: further evidence for tectonic accretion?, *Physics of the Earth and Planetary Interiors* (2008), doi:10.1016/j.pepi.2009.09.002

Stratigraphy of the Archean western Superior Province from P– and S–wave receiver functions: further evidence for tectonic accretion?

D.A. Angus [a,1,*], J–M. Kendall [a], D.C. Wilson [b,2] D.J. White [c], S. Sol [d], & C.J. Thomson [e]

[a] *Department of Earth Sciences, Wills Memorial Building, University of Bristol, Bristol, BS8 1RJ, UK*

[b] *University of Texas, Department of Geological Sciences, Austin, TX, USA*

[c] *Geological Survey of Canada, Ottawa, Ontario, Canada*

[d] *Department of Earth & Environmental Sciences, Lehigh University, Bethlehem, PA, USA*

[e] *Schlumberger Cambridge Research, Cambridge, UK*

Abstract

The Archean western Superior Province in Canada represents the nucleus of the North American continent whose origin has been speculated to be the result of widespread crustal accretion some 2.7 Ga ago. In this paper, crustal and upper–mantle seismic discontinuities beneath the western Superior Province of the Canadian shield are imaged with teleseismic P–to–S and S–to–P converted phases using the receiver function method. Three crustal discontinuities are observed: the Moho, ranging in depth between 38 and 47 km and dipping to the south; and two intra–

crustal discontinuities having depths of approximately 15 and 30 km. The crustal discontinuities undulate laterally and often lose continuity, possibly indicating an imbricated structure and/or regions of velocity gradients. In the shallow lithosphere, a positive discontinuity is imaged at approximately 65 km depth and is consistent with earlier refraction and wide–angle reflection results. Additionally, two zones of negative receiver function amplitudes at 55 km depth are observed and are coincident with a region of anomalous tomographic low P– and S–wave velocities as well as a zone of high electrical conductivity. The images for the crust and shallow upper–mantle, when integrated with previous geophysical studies, are consistent with ideas of continental root formation due to imbrication of Archean subducted material and accretion of island arcs observed in surface geology.

Key words: Archean craton, converted waves, crust, lithosphere, P– and S–waves, seismic discontinuity, receiver function.

1 Introduction

Archean cratons display a remarkable resistance to both tectonic deformation and thermal erosion. This resistance requires that the cratonic (or mantle) root be intrinsically buoyant to ensure gravitational stability, be more refractory than the adjacent asthenosphere and consist of material that has an elevated solidus temperature (Hoffman, 1990). Geological data, such as geothermal and structural measurements (e.g., Park, 1982; Hoffman, 1990), have suggested

* Corresponding author.
Email address: d.angus@bristol.ac.uk (D.A. Angus).
[1] Now at: University of Leeds, Leeds, UK
[2] Now at: Hawaiian Volcano Observatory, United States Geological Survey, Hawaii National Park, Hawaii, USA

that Archean tectonic processes may be inconsistent with present–day plate–tectonic processes. For example, Artemieva & Mooney (2002) propose that due to the higher temperatures in the Archean, the mantle would have been less viscous resulting in lower basal erosion of the cratonic lithosphere and thus promoting the preservation of the relatively thick Archean cratons. However, geological data acquired over the past few decades have indicated that Archean tectonics may not have been much different from present day processes. For instance, Moyen et al. (2006) provide evidence for a geothermal gradient of approximately 15° C/km for the Barberton Archean accretionary prism, South Africa, which is consistent with recent subduction zone geothermal gradients. The main arguments for differing tectonic processes have centred around the apparent lack of preserved ophiolites and eclogites (the presence of which are accepted as evidence for sea–floor spreading and subduction), and differing geometry of Archean terrains to more recent terrains (e.g., dip of subduction). If the existence of ophiolite analogues in Archean greenstone belts is indicative of sea–floor spreading, the rates and geometry of Archean plate movements remain to be understood (Helmstaedt & Schulze, 1989). Thus, compounded by our limited knowledge of Earth processes occurring some 2 to 4 Ga ago and the possibility that post–Archean tectonic forces may have modified preserved Archean fabrics (Culshaw et al., 2006), Archean tectonics remain somewhat of an enigma. Understanding the origin and stability of Archean terrains (or cratons) has been and still is a persistent puzzle in the study of tectonic processes in the early Earth.

There are various theories for the origin and evolution of Archean lithosphere, such as cyclical differentiation and collisional thickening (Jordan, 1988), collision of depleted island arcs (Ashwal & Burke, 1989), shallow subduction and

imbrication (Helmstaedt & Schulze, 1989) and basal accretion by cooling asthenospheric material (Thompson et al., 1996). Each model displays similar and differing physical characteristics which can be tested using various geophysical methods (Jones et al., 2001). The North American craton consists of a cluster of Archean microcontinents centred on the Canadian shield, of which most of the crust is Precambrian in age originating in the Archean (*circa* 2.5–4 Ga). Regions such as the Slave and Superior provinces are ideal natural laboratories in the study of Archean tectonics and so have been the focus of multi–disciplinary scientific research studies such as Lithoprobe (Clowes et al., 1984).

The Superior Province of North America represents the largest preserved Archean craton on Earth and is believed to be the result of a widespread crustal accretionary event that occurred *circa* 2.7 Ga (Hoffman, 1990). It is characterised by east–west trending meta–sedimentary, meta–plutonic and granitoid–greenstone subprovinces (see Kendall et al., 2002, and references therein). Earlier lithospheric studies of the Canadian Shield indicate a fast mantle lithosphere (or lid) approximately 120 to 150 km thick overlying a low velocity mantle to a depth of 300 km (e.g., Brune & Dorman, 1963; Grand & Helmberger, 1984) and anisotropic fabric to depths of 200 km oriented in the direction of surface geological strike. More recent seismic images show that these roots can extend to depths > 300 km (e.g., Silver & Chan, 1988; van der Lee & Nolet, 1997). Crustal imaging from seismic refraction data identified a two layer crust, having an upper–crustal thickness ranging between approximately 15 and 20 km and a lower–crustal depth between approximately 30 and 45 km (e.g., Hall & Hajnal, 1969; Young et al., 1986). There is also evidence of dipping crustal and lithospheric layers (e.g., Calvert et al., 1995; Rondenay

et al., 2000; Bank et al., 2000; Calvert et al., 2004; Eaton et al., 2006).

To refine these structural models of the Canadian shield, several experiments were conducted as part of the Canadian Lithoprobe Western Superior Transect (WST) (White et al., 1998). These experiments consisted of a deep seismic reflection profiling (White et al, 2003), the Teleseismic Western Superior Transect (TWiST) broadband deployment (Kay et al., 1999b; Sol et al., 2002; Kendall et al., 2002), a seismic refraction and wide–angle reflection (RWAR) survey (Kay et al., 1999a; Musacchio et al., 2004), and several magnetotelluric (MT) surveys (Ferguson et al., 2005) (see Figure 1). In this paper, we apply both the P– and S–wave receiver function method to digitally recorded broadband seismograms from the TWiST experiment to image the crust and upper–mantle structure of this Archean craton. Data from four FedNor stations (Frederiksen et al., 2007) are also included to augment the relatively limited TWiST data set. These images are compared with earlier published results from the WST transect and the results are scrutinised in terms of the various theories of Archean lithospheric origin and evolution. Even with the limited data, the combined P– and S–wave receiver function imaging approach yields consistent results with those from other geophysical analysis. This consistency suggests that application of receiver function CCP imaging for 2–D broadband seismic experiments deployed for much greater time has potential to produce relatively inexpensive images of the crust and lithosphere compared to higher resolution active–source deep seismic reflection and refraction surveys.

2 Previous geophysical studies of the western Superior transect

Various teleseismic techniques have been applied to data acquired from the TWiST broadband seismic experiment. Surface wave studies indicate a thick continental root extending to a depth of greater than 200 km, with a thin high–velocity layer (with thickness ranging anywhere between 5 and 20 km) underlying a crust with a thickness of roughly 40 km (Kendall et al., 2002). SKS–splitting analysis reveals moderate to large shear–wave splitting, with fast polarisation aligned along strike of the east–west trending regional geological boundaries and current absolute plate motion (Kay et al., 1999b; Frederiksen et al., 2007). From traveltime body–wave tomography, both a high– and low–velocity anomaly are imaged, extending deep into the mantle (Sol et al., 2002; Kendall et al., 2002).

Within the vicinity of the TWiST array, controlled–source deep seismic reflection as well as refraction/wide–angle reflection experiments were also conducted (e.g., see NS and EW lines in Figure 1). Moho reflection imaging from PmP and SmS phases shows a southward deepening Moho with depths ranging between approximately 39 km and 42 km, average P– and S–wave velocities of 6.6 and 3.8 km/s, and an average V_P/V_S ratio of 1.75 (Kay et al., 1999a). Musacchio et al. (2004) performed detailed integrated modelling of RWAR and gravity data. They observe a thick crust with an average thickness of roughly 40 km and consisting of several prominent intra–crustal seismic boundaries attributed to compositional layering, with felsic and greenstone rocks at shallow depths and granitoid rocks in the lower crust. Musacchio et al. (2004) also observe a northward dipping upper–mantle discontinuity at approximately 60 km as well as a deep boundary at a depth of roughly 120 km. Both reflection

and refraction analysis indicate dipping layers within the crust (e.g., Calvert et al., 1995; White et al, 2003; Musacchio et al., 2004; Zeng & Calvert, 2006).

The several MT surveys of the WST (see black triangles in Figure 1) show the alignment of long–period geoelectric strike azimuths sub–parallel to the east–west metamorphic fabric (Ferguson et al., 2005) and are consistent with the SKS shear–wave splitting fast direction. Ferguson et al. (2005) also reveal a broad and shallow region of resistive crust in the northern section and a deeper conductive anomaly located within the mid–section of the TWiST array at a depth of approximately 50 km. The regions of low and high conductivity appear to agree with the regions of low and moderate heat flow (Rolandone et al., 2003).

3 Data and method

The receiver function method yields an estimate of Earth structure in terms of a sequence of time offset mode conversions from sub–vertically propagating incident (or primary) waves (e.g., Langston, 1977). This is accomplished by deconvolving instrument response as well as source and path effects from recorded three–component data to emphasise sub–horizontal seismic discontinuities using converted body–wave (P– and S–wave) energy. The method is conceptually simple and relies on the fact that pre–cursory (i.e., S–to–P converted) and post–cursory or coda (i.e., P–to–S converted) phases originate from sub–horizontal seismic discontinuities. In this study, we apply the receiver function method to both P–to–S and S–to–P converted phases to delineate crustal and lithospheric seismic discontinuities to depths of 100 km. We restrict the imaging depth to 100 km due to the relatively limited data.

The P–receiver function (i.e., receiver function using P–to–S converted waves) is the most commonly used approach for imaging upper–mantle structure because the primary P–wave phase is often clearly identifiable (i.e., any precursory signal is generally the combination of site and instrument noise). There are a variety of receiver function techniques available (e.g., Kind et al., 1995; Park & Levin, 2000; Helffrich, 2006) and they differ, generally, in the manner in which the instrument response and source/path effects are deconvolved. However, they effectively yield similar receiver functions that differ mainly in dominant frequency content and amplitude fidelity (e.g., Park & Levin, 2000; Hammond, 2007). One disadvantage of the P–receiver function is that deeper crustal and upper–mantle conversions are often contaminated by primary P–wave crustal multiples that can be difficult to suppress (e.g., Bostock, 1997) and can be particularly troublesome for stations located above deep sedimentary basins (e.g., Wilson et al., 2003). The S–receiver function (i.e., receiver function using S–to–P converted waves) is particularly attractive because the converted phases do not to suffer from contamination by multiply reflected primary S–wave phases, which arrive later than the faster propagating S–to–P converted phases (e.g., Li et al., 2004; Kumar et al., 2005; Yuan et al., 2006; Angus et al., 2006; Rychert et al., 2007). However, care must be taken when using S–receiver functions due to possible interference from later arriving teleseismic P–wave energy, such as pPPP and pPPPP teleseismic phases (e.g., Bock & Kind, 1991; Wilson et al., 2006).

For our receiver function analysis, we use the teleseismic data recorded by the TWiST array. This experiment consisted of 14 temporary seismic broadband stations deployed along a north trending line approximately 480 km long in the Superior Province, Ontario, Canada, and three additional stations located

to the north in the Archean–Proterozoic transition (see Figure 1). Over a period from May to November 1997, approximately 1100 globally–distributed earthquakes were recorded. To increase the number of events in the data set, we use data from four FedNor (Federal Economic Development Initiative for Northern Ontario) seismic network stations that fall within the vicinity of the TWiST array.

For the P–wave receiver function analysis, waveforms from a subset of over 100 earthquakes having magnitudes (mb) $\geq$ 5.0 and epicentral distances ranging from 30° and 95° were used. The waveforms were filtered between 1/30 and 4 Hz and rotated into theoretical ray coordinates (P, Sv and Sh components) using a 1–D velocity model based on Musacchio et al. (2004) for the upper 120 km and IASP91 (Kennett & Engdahl, 1991) below 120 km. To filter out signals with weak P component, P–receiver functions were evaluated only for P–wave signals with a signal–to–noise ratio (SNR) $\geq$ 3 on the P component. To estimate the source wavelet, a time window of 150 seconds was applied around the direct P–wave arrival on the P component using a 5 second Hamming taper (the beginning of the window was set to 30 seconds prior to the theoretical P–wave arrival time). Deconvolution was performed in the frequency domain, with an optimum water level based on a tradeoff between data fit and minimal receiver function ringing (Wilson et al., 2006). A total of 316 P–wave receiver functions were evaluated from 85 earthquakes (see grey circles in Figure 2).

For the S–wave receiver function analysis, we followed the approach of Wilson et al. (2006) to ensure that the S–receiver functions are free from contamination by interfering primary P–wave energy. A subset of over 50 earthquakes having magnitudes (mb) $\geq$ 5.0, epicentral distances between 55° and 80°, and depths $\leq$ 400 km were used. It is important to note that although Wilson et

al. (2006) suggest that events should be limited to epicentral distances between 60° and 75° and depths $\leq$ 300 km, to increase the number of S–receiver functions we expanded the range of epicentral distances between 55° and 80° and depths to $\leq$ 400 km. Comparison of S–receiver images for three epicentral distance ranges shows that expanding epicentral distances results in minimal change in crustal and shallow sub–crustal structure while increasing coverage of the deeper sub–crust (see Figure 5). The waveforms were filtered between 1/40 and 4 Hz and rotated into theoretical ray coordinates using the 1–D velocity model applied in the P–receiver function analysis. To filter out signals with weak Sv component, S–receiver functions were evaluated only for S–wave signals with a SNR $\geq$ 2. A lower SNR threshold was applied because the S–wave signals were noticeably noisier than the P–wave signals. Similar to the P–receiver function, deconvolution was performed in the frequency domain, with the source wavelet estimated using a 18 s time window applied around the direct S–wave arrival on the Sv component. A total of 50, 67 and 88 S–wave receiver functions over a time window of 80 s were obtained for epicentral distances between 60°–75°, 57.5°–77.5° and 55°–80°, respectively, from over 50 earthquakes (see black circles in Figure 2). Table 1 shows the distribution of P– and S–wave receiver functions for the TWiST and FedNor seismic stations.

To transform the receiver function data into offset and depth space, we apply the common–conversion–point (CCP) imaging, which is a converted–phase analogue to the common–depth–point (CDP) imaging used in reflection seismology (e.g., Dueker & Sheehan, 1998; Angus et al., 2006). Specifically, the P– and S–receiver functions are backprojected along the theoretical ray path using the 1–D velocity model discussed earlier, and stacked into lateral and

vertical depth bins. Since the average station spacing along the TWiST array was 30 km, receiver function amplitudes were stacked along ray paths with an initial lateral bin radius of 40 km and scaled according to the Fresnel zone with increasing depth. To reduce the effects of receiver function noise, each imaging bin was a weighted average of all receiver function rays which passed within 40 km laterally of that imaging point. It should be noted that when significant lateral velocity heterogeneity exists, the mapping of receiver function energy via the CCP approach may not represent the most accurate focusing for true Earth structure. However, the CCP imaging method should provide an adequate geometric image of crustal and upper–mantle discontinuities, at least to first–order (Wilson et al., 2003).

4 Receiver function observations

4.1 P–wave Receiver Functions

Figure 3 displays CCP image sections for the individual Ps, PpPs and PpSs converted phases to depths down to 100 km and latitudes between 48° and 54° N. A positive amplitude is shown in red and indicates a positive seismic impedance change with depth. [Note that the polarity of the PpSs receiver functions are reversed to match those of the Ps and PpPs receiver functions.] The Moho dips to the south with an average depth of 42 km and appears to be discontinuous (i.e., vertical step) around latitude 49.75° N. There are also indications of two intra–crustal discontinuities at depths of approximately 15 km and 30 km, also dipping to the south. There are indications of a positive seismic discontinuity at depth of approximately 65 km and two negative

discontinuities at 55 km.

In Figure 4(top), the individual Ps, PpPs and PpSs CCP images are combined to enhance coherent physical signals and reduce noise generated by improper CCP imaging (top). Also shown (below) is an interpreted section. Comparing Figures 3 and 4, it can be seen that the stacked CCP image in Figure 4 yields visibly more coherent seismic discontinuities. The Moho is more prominent with an average depth of 42 km and dipping to the south. The two intra–crustal discontinuities are also more clearly visible at roughly 15 km and 30 km depth. However, due to poor ray coverage below latitudes 48.5°–48.75° N and 53°–53.25° N, the mid–crustal discontinuities and Moho can only be extrapolated within these regions (see ray coverage plot at bottom in Figure 3).

The sub–Moho discontinuities at 55 km depth appear to be enhanced marginally between latitudes 50.25° and 52.5° N. Both these shallow sub–crustal discontinuities are zones of large negative receiver function amplitudes (blue), indicated by the LVZ symbol. The LVZ zones are imaged above the positive discontinuity at 65 km depth and suggest a region of low mantle velocity consistent with the RWAR results of Musacchio et al. (2004). Another interesting feature is the region of diffuse positive receiver function amplitudes highlighted by the two dashed–dotted lines to the left of the LVZ in Figure 4 between 48° and 49.75° N. This feature appears to deepen from approximately 52 km at 48° N to 57 km at 49.7° N.

4.2 S–wave Receiver Functions

CCP image sections are generated for Sp converted phases to depths down to 100 km and latitudes between 48° and 54° N. To facilitate comparison with the P–receiver function images, the polarities of the S–receiver functions are reversed (as was done for the PpSs converted phases in the P–receiver function method). Thus a negative amplitude is shown in red and indicates a positive seismic impedance change with depth. Since S–to–P converted phases have lower frequency content relative to P–to–S converted phases, the S–receiver function CCP images have lower vertical resolution when compared to the P–receiver function CCP images (i.e., the Sp images appear smoother).

In Figure 5, Sp CCP images are compared for source–receiver epicentral distance restrictions of 60°–75° (top panel), 57.5°–77.5° (second from top panel) and 55°–80° (second from bottom panel), and ray coverage for epicentral distances of 55°–80° (bottom panel). Restricting events to 60°–75° [as suggested by Wilson et al. (2006)] yields a total of 50 S–receiver functions (see top panel). At crustal depths, the sparsely imaged discontinuity at approximately 40 km depth represents the Moho converted Sp phase. Since the signals are much broader than those from the P–receiver function, it is difficult to clearly observe any intra–crustal discontinuities. Expanding the epicentral distances to 57.5°–77.5°, a total of 67 receiver functions are evaluated. The Sp image displays similar characteristics to that of the top panel, with the exception of a marginal improvement in Sp CCP image coverage. There appears to be an observable positive velocity contrast at approximately 65 km depth and this is consistent with the discontinuity observed at 65 km in Figure 4. There is also a prominent low velocity anomaly at roughly 60 km depth between latitudes

50° and 52° N. Further expanding the epicentral distance range to 55°–80° yields 88 S–receiver functions. In this image, the Moho and sub–crustal discontinuities are imaged more coherently laterally due to the further increase in ray coverage. Since all three CCP images show similar trends, we have chosen to use the CCP image for events between 55° and 80° in the rest of our analysis, as it provides a more complete S–receiver function image. Given that we are restricting the depth of imaging to less than 100 km, interference from precursory teleseismic P phases are likely to be minimal.

4.3 Combined P– and S–wave Receiver Functions

Figure 6 shows the combined P– and S–receiver function images (top) as well as an interpreted image (below). The interpretation compares well with that of the stacked P–receiver functions shown in Figure 4. Due to the differing frequency content of the P– and S–receiver functions, a direct comparison is difficult to interpret. However, stacking the P– and S–receiver functions does help provide some additional constraints in terms of reducing receiver function noise by summing coherent signals and, more importantly, increasing ray coverage. The Moho is seen through much of the image, dipping from north to south and having an average depth of 42 km. The two intra–crustal discontinuities are also visible with average depths of approximately 15 km and 30 km. Due to poor ray coverage in the shallow crust around 48.5° and 53° N, the intra–crustal discontinuities can only be inferred. The laterally discontinuous Moho inferred in Figure 3 near 49.75° N is again visible, though not as prominently. The sub–Moho discontinuity at approximately 65 km between 49.75° and 53.5° N can be extrapolated northward. The LVZ zones above the

shallow sub–crustal discontinuity are also still present. With the addition of the S–receiver functions, the region of low velocity is observed to be laterally slightly more continuous between 50° and 52°N.

Also shown in Figure 6 is the region between 48° and 50° N highlighted by two dashed–dotted lines and a question mark symbol discussed earlier (see Figure 4). Musacchio et al. (2004) interpret a complex structure for this region: a high velocity anisotropic lower–crustal layer having thickness of approximately 20 km to the south and pinching out towards the north at approximately 51°N. They interprete this layer to consist predominantly of amphibolite, having oceanic crustal origin, and forming a north dipping suture between oceanic and continental crust.

Musacchio et al. (2004) image a northward dipping oceanic mantle slab, initially horizontal between latitudes 48° and 49° N with depth of 50 km and dipping shallowly to a depth of 80 km between latitudes 49° and 52° N. Although the CCP receiver function images highlight a discontinuity at 65 km depth, there is little evidence that this layer dips northward as interpreted by Musacchio et al. (2004). However, due to the lower frequency of teleseismic signals with respect to controlled source seismic signals, it is possible that the receiver function technique is not capable of imaging such a low angle dipping structure over the small lateral distance of the array (approximately 500 km). Thus, it is entirely possible that these features do exist but due to the lower frequency of the teleseismic converted waves it is difficult to unravel the finer structure. It is also interesting to examine the regions highlighted by 'G' (for velocity gradient) shown in the stacked P– and S–receiver function image (Figure 6). These regions of diffuse or weak converted wave signals are consistent with the velocity gradients observed in the RWAR results of Musacchio et al.

(2004).

4.4 Scrutinizing the CCP images

To validate the CCP imaging technique we apply the H–κ stacking method (Zhu & Kanamori, 2000) to estimate Moho depth and V_P/V_S ratio across the entire array. Before applying the H–κ stacking approach, we reprocess the P–wave data using the extended–time domain multitaper frequency domain cross–correlation (ETDF) method of Helffrich (2006). This allows a comparison of Moho depth estimates based on different deconvolution and imaging methods (i.e., spectral deconvolution with CCP imaging versus ETDF deconvolution with H–κ stacking). Furthermore, the results can be compared with the controlled source RWAR results of Kay et al. (1999a) and Musacchio et al. (2004).

The reprocessed P–wave data were filtered between 1/5 and 5 Hz and rotated into theoretical backazimuthal coordinates (radial, tangential and vertical) using the AK135 1–D velocity model. The receiver functions were calculated using a cutoff frequency (Park & Levin, 2000) of 1.0 Hz. The ETDF deconvolution was only performed on signals with clear P–wave arrival. A total of 351 P–wave receiver functions with clear, impulsive arrival at zero time lag on the vertical component were evaluated. The bracketed numbers in Table 1 represent the number of P–receiver functions for each station using the ETDF method.

For the H–κ stacking, the depth of the Moho and V_P/V_S ratio were estimated using an average P–wave crustal velocity of 6.5 km/s (based on Musacchio et

al., 2004) and a phase weighting of 65%, 35% and 0% for the Ps, PpPs and PsPs/PpSs phases, respectively. Figure 7 displays the results of the H–κ stack for the FedNor station MUMO. The H–κ stack for MUMO estimates the Moho depth to be 39.2 ± 0.7 km with an average crustal V_P/V_S ratio of 1.71 ± 0.04. This result is consistent with the CCP images, the RWAR results of Kay et al. (1999a) and Musacchio et al. (2004), and the H–κ stack of Darbyshire et al. (2007). Table 1 summarizes the results for all stations and in Figure 6(bottom) the H–κ Moho depths are plotted as plus symbols below the corresponding station. The Moho depth decreases from approximately 47 km in the south to 39 km in the north, with mean of 41.7 km. The V_P/V_S ratio is relatively constant across the array, with mean of 1.74.

Figure 8(top) displays the raw radial receiver functions as a function of epicentral distance for the FedNor station MUMO. The Moho conversion is clearly visible at 5 s along with the multiple PpPs at 16 s. The multiples PsPs and PpSs are not visible at their predicted arrival time of 21 s and this is the reason we apply 0% phase weighting for these phases in the H–κ stacking. Also visible on the raw P–receiver function traces is a positive phase at approximately 10 s which corresponds to the CCP imaged discontinuity at 65 km. In Figure 8(bottom), the P–wave receiver functions for MUMO are stacked using a jackknife averaging scheme (Efron, 1982; Hammond, 2007) which allows an estimate of the standard deviation of the receiver function stack. Since there are only 30 P–wave receiver functions for MUMO we apply the stack over all epicentral distances and backazimuths. The stack clearly indicates positive anomalies for the Moho conversions: Ps, PpPs and PsPs+PpSs (weak). However, the stack also shows a significant negative anomaly at approximately 6-8 s which corresponds to the LVZ imaged at 55 km depth. As well, although

weak, there is a positive anomaly at approximately 10 s which corresponds to the imaged positive discontinuity at 65 km depth.

5 Interpretation

A simplified summary of the crustal and upper–mantle structure beneath the TWiST array from previous geophysical studies is shown in Figure 9 (top panel). Heat flow measurements of Rolandone et al. (2003) indicate low heat flow (≤ 20 mW m^{-2}) around 48° and 52° N, and moderate heat flow (≈ 40 mW m^{-2}) around 49° N. From MT measurements, Ferguson et al. (2005) observe a resistive ($> 10000\ \Omega\cdot$ m) shallow (≈ 20 km) region centred below latitude 52° N (region highlighted in magenta) and a deeper (centred at roughly 50 km depth and having radius of approximately 40 km) electrically conductive body ($< 10\ \Omega\cdot$ m) located below latitude 51° N (region highlighted in yellow). The regions of low and moderate heat flow appear to coincide with the regions of low and high electrical conductivity.

Also shown is the crustal and shallow sub–crustal structure interpreted from RWAR data of Musacchio et al. (2004). The crust has an average thickness of 45 km and is observed to consist of three crustal layers. They interpret these as an upper crust composed of felsic and mafic intrusives, a middle crust and a lower oceanic crust. The crust displays lateral heterogeneity associated with crustal suturing as well as regions or pockets of perhaps subduction–related mafic intrusions within the lower crust in the northern section of the array (see Nitescu et al., 2006). An imaged sub–crustal layer dipping northward from approximately 45 km to 80 km depth is interpreted to be of oceanic mantle origin (formed mostly of depleted Harzburgite). Musacchio et al. (2004) also

observe a deeper sub–crustal reflection around 110 km depth. The tomography results of Sol et al. (2002) indicate two elongate regions of anomalous velocities; a high–velocity region centred below 49° N at depth of 160 km and a low–velocity region centred below 50° N at 140 km depth.

Included to the right is a shear–wave velocity model compiled from surface wave modelling (see Kendall et al., 2002; Darbyshire et al., 2007). Five velocity discontinuities are observed with the Moho at about 40 km depth and shallowing to the north (Darbyshire et al., 2007) as well as an intra–crustal layer at 20 km depth. Both a shallow and deep sub–crustal step are observed at 60 km and 120 km. The shallow 5 to 20 km thick sub–crustal layer at 60 km depth agrees with Musacchio et al. (2004). It is important to note that both Frederiksen et al. (2007) and Darbyshire et al. (2007) observe significant lateral variability within the lithosphere of the Superior Province and so it is expected that the depth estimate for the Western Superior Province differ from the regional average. The grey region shows the range of acceptable solutions from the surface–wave shear–wave velocity inversion (Kendall et al., 2002; Darbyshire et al., 2007), suggesting possible additional discontinuities at approximately 80 and 100 km depth.

To put the above results into context it is helpful to look at results obtained for the geographically proximal Archean Slave Province of similar age. Snyder & Bruneton (2007) observe a crustal thickness of approximately 45 km as well as two deep sub–crustal layers at depths of 70 and 150 km. In this same region of the Slave Province, Bostock (1997) images deep sub–crustal discontinuities at 75, 135 and 195 km depth with characteristic shallow dips. Based on the geometry, sharpness and anisotropy of the discontinuities, Bostock (1997) suggests a structural origin to the vertical heterogeneity, such as

shallow subduction.

Also shown in Figure 9 (bottom panel) is a simplified interpretation of the crustal and upper–mantle structure based on the P– and S–receiver function images. The crust shows similar complexity with Moho thickness averaging around 42 km and consisting of three layers. The lack of lateral continuity of the imaged crustal phases and observed dip of the lower layers may reflect an imbricated crustal structure and/or presence of velocity gradients. The dashed line in the lower crust between 49° and 51° N hints at the presence of a crustal suture zone as seen in Musacchio et al. (2004), but not resolved with certainty in the receiver function images. A sub–crustal structure (grey layer in bottom of Figure 9) is also observed and appears to be consistent with the sub–crustal oceanic mantle interpreted by Musacchio et al. (2004). However, it is not clear from the receiver function images whether this discontinuity touches the base of the crust in the southern region for latitudes less then 49.75° N (i.e., a region of mantle underplating). Regions of low velocity lie on either side of this slab like structure. The low–velocity region beneath this structure coincides with the conductive zone observed in the MT data as well as the low–velocity anomaly observed in the tomography results.

A discontinuity at depth of 80 km is weakly visible in the CCP images. The existence, origin and nature of this discontinuity is not clear. At these depths, the receiver function images become progressively noisier and appear to be affected by improper CCP imaging artifacts (e.g., signal noise and crustal reverberations). However, this discontinuity may not be entirely due to noise and may reflect actual physical sub–crustal heterogeneity similar to the results observed by Bostock (1997).

It should be noted that the absolute depths of the imaged crustal and lithospheric seismic discontinuities are controlled primarily by the inferred CCP 1–D velocity model and to a lesser degree the estimated source–receiver ray–theoretical incidence angles. Although the choice of 1–D velocity model will control the depth estimates, the geometry will remain relatively unchanged (Angus et al., 2006). Improvements to the first–order CCP imaging would require the positioning of receiver functions into offset and depth using a 2– or 3–D velocity model as well as migration via a Kirchhoff (e.g., Wilson & Aster, 2005) or ray/Born (e.g., Bostock & Rondenay, 1999) approach. Using a more realistic velocity model (e.g., 2–D) in the CCP imaging approach would include the effects of lateral structural heterogeneity and would improve focusing of the converted wave energy. Furthermore, if sufficient data existed, migration could be applied which would allow for the proper focusing of diffracted and multiple reflected energy. However, due to the limited duration of the TWiST deployment, there is an insufficient amount of broadband teleseismic data for proper migration. It should be noted that the imaged depths are within the range of those estimated from other geophysical techniques and, furthermore, the geometry shows similar consistency with previous crustal and lithospheric studies of the Canadian Shield.

6 Discussion

The primary purpose of our receiver function study was to help place constraints on the origin and evolution of the western Superior craton in terms of the various theories of Archean tectonics. It is interesting to note that our P– and S–receiver function images for the WSP display a geometry consistent with

other seismic results (i.e., seismic reflection and refraction/wide–angle reflection data) and point toward undulating (possibly imbricated) sub–horizontal and shallow dipping crustal and upper–mantle. Furthermore, the question of whether these studies provide evidence of shallow subduction and suturing within the WSP is key. This is because shallow subduction is a main feature of the Helmstaedt & Schulze (1989) Archean tectonic accretion model, where the higher heat loss from the Archean Earth was accomplished by faster spreading rates and shallow subduction of younger and more buoyant oceanic lithosphere. However, it is important to examine our results in the context of all theories for the origin and evolution of Archean lithosphere.

The basal accretion model of Thompson et al. (1996) is based on thermal conductivity measurements in the Slave Province, where past geothermal gradients are reconstructed from present day thermal measurements and metamorphic history. Thompson et al. (1996) conclude that the lithosphere was thin (< 100 km) in the Archean, possibly due to lithospheric delamination, and thickened progressively via basal accretion of cooling asthenospheric material. The characteristic lateral varying structures within the sub–crust is inconsistent with the basal accretion model, where it is expected that the lithospheric root would not display any characteristic lateral heterogeneity.

The cyclical differentiation and thickening model of Jordan (1988) suggests that the origin of Archean cratons is due to periods of continent–continent collision, where the formation of thick lithosphere results from advective thickening during successive major episodes of compressional orogens (i.e., crust accretion is coincident with a progressive lithospheric thickening). If we accept that the imaged sub–crustal layering is dipping and related to oceanic subduction processes, the model of Jordan (1988) appears to be inconsistent

with the geophysical results from both the RWAR and receiver function analysis (at least in the WST). However, if the layering is not interpreted to be subducted oceanic fragments, but rather a result of advective layering and/or shear banding, the model of Jordan (1988) remains plausible.

Ashwal & Burke (1989) propose a model that involves repeated collision of depleted island arcs; detachment of depleted mantle lithosphere from overlying crust and replacement by less depleted asthenospheric mantle; thinning of the crust via erosion, rifting, and isostatic uplift; and subsequent alkaline Cenozoic volcanism. Helmstaedt & Schulze (1989) propose a model that involves repeated accretion of depleted island arcs with progressive thickening of the lithosphere by underplating of shallow subducted lithosphere, but without the lithospheric detachment suggested by Ashwal & Burke (1989). In this model, the higher heat loss from the Archean Earth is accommodated through faster spreading than present day ocean–ridge spreading rates, resulting in shallow or low angle subduction and subsequent imbrication of subducted oceanic slab material. The presence of ophiolites provide evidence for oceanic island arc accretion, where lateral underplating of continent by oceanic lithosphere is accomplished by imbrication of upper portions of the oceanic lithosphere. Both the lithospheric detachment model (Ashwal & Burke, 1989) and the shallow subduction and accretion model (Helmstaedt & Schulze, 1989) are consistent with characteristic layering observed in the RWAR and receiver function analysis. However, the requirement for lithospheric detachment in the model of Ashwal & Burke (1989) is not consistent with the deep continental root observed in the various surface wave analyses for the WSP. The Helmstaedt & Schulze (1989) model is further supported by the fact that the measured shear–wave splitting fast polarisation direction (Kay et al., 1999b)

and long–period geoelectric strike azimuths (Ferguson et al., 2005) are sub–parallel to the regional geological boundaries and consistent with lithospheric fabric being accrued during the Archean.

As part of Lithoprobe, the results from the WST have provided some constraints in our understanding of the origin and evolution of the Archean crust and lithosphere. Unfortunately, the relatively short deployment of the TWiST array has limited the analysis of the subsurface below the Archean western Superior Province. However, more recent geophysical experiments within the Canadian shield are contributing greatly to these earlier experiments. The POLARIS (Portable Observatories for Lithospheric Analysis and Research Investigating Seismicity) deployment is providing not only vast quantities but also remarkable quality geophysical data throughout the Canadian shield (see http://polaris.es.uwo.ca). The HuBLE (Hudson Bay Lithospheric Experiment) teleseismic experiment, an international collaborative project consisting of scientists from Canada, Germany and the UK, is currently investigating the lithospheric structure and seismicity of the Hudson Bay region to test hypotheses of Archean root formation and the persistence of intracratonic basins (e.g., Thompson et al., 2008). With longer deployment times, larger arrays and improved quality of data, it is expected that more refined geophysical images will help place further constraints on the geometry of the Archean craton in the Superior Province and improve our understanding of the origin and evolution of Archean tectonics.

7 Acknowledgments

The authors would like to thank Andrew Frederiksen and two anonymous reviewers for comments on the manuscript. D.A.A. and J–M.K. thank Dave Eaton for helpful discussion of the results. The receiver function analysis was performed using Matlab®, the SAC toolkit for Mac O/S as well as various receiver function programs provided by George Helffrich. All figures were produced using both Matlab® and GMT (Wessel & Smith, 1995). TWiST was funded by Lithoprobe (NSERC–Canada), the Royal Society of London, NERC grant GR9/03469, Monopros Ltd, and the Geological Survey of Canada.

References

Angus, D. A., Wilson, D. C., Sandvol, E. and Ni, J. F. (2006) Lithospheric structure of the Arabian and Eurasian collision zone in eastern Turkey from S–wave receiver functions, *Geophys. J. Int.*, **166**, 1335–1346.

Artemieva, I. M. and Mooney, W. D. (2002) On the relations between cratonic lithosphere thickness, plate motions, and basal drag, *Tectonophysics*, **358**, 211–231.

Ashwal, L. D. and Burke, K. (1989) African lithospheric structure, volcanism, and topography, *Earth Planet. Sci. Lett.*, **96**, 8–14.

Bank, C–G., Bostock, M.G., Ellis, R.M. and Cassidy, J.F. (2000) A reconnaissance teleseismic study of the upper mantle and transition zone beneath the Archean Slave craton in NW Canada, *Tectonophysics*, **319**(3), 151–166.

Bock, G. and Kind, R. (1991) A global study of S–to–P and P–to–S conversions from the upper mantle transition zone, *Geophys. J. Int.*, **107**, 117–129.

Bostock, M. G. (1997) Anisotropic upper–mantle stratigraphy and architecture of the Slave craton, *Nature*, **390**, 392–395.

Bostock, M. G. and Rondenay, S. (1999) Migration of scattered teleseismic body waves, *Geophys. J. Int.*, **137**, 732–746.

Brune, J. and Dorman, J. (1963) Seismic waves and earth structure in the Canadian Shield, *B.S.S.A.*, **53**, 167–210.

Calvert, A. J., Cruden, A. R. and Hynes, A. (2004) Seismic evidence for preservation of the Archean Uchi granite–greenstone belt by crustal–scale extension, *Tectonophysics*, **388**, 135–143.

Calvert, A. J., Sawyer, E. W., Davis, W. J. and Ludden, J. N. (1995) Archaean subduction inferred from seismic images of a mantle suture in the Superior Province, *Nature*, **375**, 670–674.

Clowes, R.M., Green, A.G., Yorath, C.J., Kanasewich, E.R., West, G.F. and Garland, G.D. (1984) LITHOPROBE – a national program for studying the third dimension of geology, *J. Can. Soc. Expl. Geophys.*, **20**, 23–39.

Culshaw, N. G., Beaumont, C. and Jamieson, R. A. (2006) The orogenic superstructure–infrastructure concept: Revisited, quantified, and revived, *Geology*, **34**(9), 733–736.

Darbyshire, F. A., Eaton, D. W., Frederiksen, A. W. and Ertolahti, L. (2007) New insights into the lithosphere beneath the Superior Province from Rayleigh wave dispersion and receiver function analysis, *Geophys. J. Int.*, **169**, 1043–1068.

Dueker, K. G. and Sheehan, A. F. (1998) Mantle discontinuity structure beneath the Colorado Rocky Mountains and High Plains, *J. Geophys. Res.*, **103**, 7153–7169.

Eaton, D. W., Dineva, S. and Mereu, R. (2006) Crustal thickness and Vp/Vs variations in the Grenville orogen (Ontario, Canada) from analysis of tele-

seismic receiver functions, *Tectonophysics*, **420**, 223–238.

Efron, B. (1982) The jackknife, the bootstrap and other resampling plans, *Society for Industrial and Applied Mathematics*, Philidelphia, Pennsylvania.

Ferguson, I. J., Craven, J. A., Kurtz, R. D., Boerner, D. E., Bailer, R. C., Wu, X., Orellana, M. R., Spratt, J., Wennberg, G. and Norton, M. (2005) Geoelectric response of Archean lithosphere in the western Superior Province, central Canada, *Phys. Earth Planet. Int.*, **150**, 123–143.

Frederiksen, A. W., Miong, S–K., Darbyshire, F. A., Eaton, D. W., Rondenay, S. and Sol, S. (2007) Lithospheric variations across the Superior Province, Ontario, Canada: Evidence from tomography and shear wave splitting, *J. Geophys. Res.*, **112**, B07318.

Grand, S. P. and Helmberger, D. V. (1984) Upper mantle shear structure of North America, *Geophys. J. R. Astr. Soc.*, **76**, 399–438.

Hales, A. L. (1969) A seismic discontinuity in the lithosphere, *Earth Planet. Sci. Lett.*, **7**, 44–46.

Hales, A. L., Muirhead, K. J. and Rynn, J. M. W. (1980) A compressional velocity distribution for the upper mantle, *Tectonophysics*, **63**, 309–348.

Hall, D. J. and Hajnal, Z. (1969) Crustal structure of northwestern Ontario: Refraction seismology, *Can. J. Earth Sci.*, **6**, 81–99.

Hammond, J. O. S. (2007) Imaging the upper mantle beneath the Seychelles: architecture of a micro–continent, Ph.D. thesis, University of Leeds, 2007.

Helffrich, G. (2006) Extended–time multi–taper frequency domain cross–correlation receiver function estimation, *B.S.S.A.*, **96**, 344–347.

Helmstaedt, H. H and Schulze, D. J. (1989) Southern African kimberlites and their mantle sample: Implications for Archean tectonics and lithosphere evolution, in *Kimberlites and related rocks, Volume 1: Their composition, occurrence, origin, and emplacement*, ed. Ross, J., Geological Society of

Australia Special Publication **14**, 358–368.

Hoffman, P. F. (1990) Geological constraints on the origin of the mantle root beneath the Canadian shield, *Phil. Trans. R. Soc. Lond. A*, **331**, 523–532.

Jones, A. G., Ferguson, I. J., Chave, A. D., Evans, R. L. and McNeice, G. W. (2001) Electric lithosphere of the Slave craton, *Geology*, **29** (5), 423–426.

Jordan, T. H. (1988) Structure and formation of the continental tectosphere, in *Oceanic and continental lithosphere; similarities and differences*, eds. Menzies, M. A. and Cox, K. G., Journal of Petrology, Special Lithosphere Issue, 11–37.

Kay, I., Musacchio, G., White, D., Asudeh, I., Roberts, B., Forsyth, D., Hajnal, Z., Koperwhats, B. and Farrell, D. (1999a) Imaging the Moho and Vp/Vs Ratio in the Western Superior Archean Craton with Wide Angle Reflections, *Geophys. Res. Lett.*, **26** (16), 2585–2588.

Kay, I., Sol, S., Kendall, J–M., Thomson, C., White, D., Asudeh, I., Roberts, B. and Francis, D. (1999b) Shear wave splitting observations in the Archean Craton of Western Superior, *Geophys. Res. Lett.*, **26** (17), 2669–2672.

Kendall, J–M., Sol, S., Thomson, C. J., White, D. J., Asudeh, I., Snell, C. S. and Sutherland, F. H. (2002) Seismic heterogeneity and anisotropy in the Western Superior Province, Canada: insights into the evolution of an Archean craton, in *The Early Earth: Physical, Chemical and Biological Development*, edited by C. M. R. Fowler et al., Geological Society, London, Special Publications, **199**, 27–44.

Kennett, B. L. N. and Engdahl, E. R. (1991) Traveltimes for global earthquake location and phase identification, *Geophys. J. Int.*, **105**, 429–465.

Kind, R., Kosarev, G. and Petersen, N. V. (1995) Receiver functions at the stations of the German regional seismic network (GRSN), *Geophys. J. Int.*, **121**, 191–202.

Kumar, P., Yuan, X., Kind, R. and Kosarev, G. (2005) The Lithosphere–Asthenosphere boundary in the Tien Shan-Karakoram region from S receiver functions – Evidence of continental subduction, *Geophys. Res. Lett.*, **32**, L07305.

Langston, C.A. (1977) Corvallis, Oregon, crustal and upper mantle receiver structure from teleseismic P and S waves, *B.S.S.A.*, **67**, 713–724.

Li, X., Kind, R, Yuan, X. Wölbern, I. and Hanka, W. (2004) Rejuvenation of the lithosphere by the Hawaiian plume, *Nature*, **427**, 827–829.

Lodge, A. & Helffrich, G. (2009) Grid search inversion of teleseismic receiver functions, *Geophys. J. Int.*, , 1–11.

Moyen, J–F., Stevens, G. and Kisters, A. (2006) Record of mid–Archean subduction from metamorphism in the Barberton terrain, South Africa, *Nature*, **442**(3), 559–562.

Musacchio, G., White, D. J., Asudeh, I. and Thomson, C. J. (2004) Lithospheric structure and composition of the Archean western Superior Province from seismic refraction/wide–angle reflection and gravity modeling, *J. Geophys. Res.*, **106**, B03304.

Nitescu, B., Cruden, A. R. and Bailey, R. C. (2006) Integrated potential–field and seismic constraints on the structure of the Archean metasedimentary English River belt, Western Superior craton, Canada, *Precambrian Research*, **144**, 261–277.

Park, R. G. (1982) Archaean tectonics, *Int. J. Earth Sci.*, **71** (1), 22–37.

Park, J. and Levin, V. (2000) Receiver functions from multiple–taper spectral correlation estimates, *B.S.S.A.*, **90** (6), 1507–1520.

Rolandone, F., Mareschal, J. C., Jaupart, C., Gosselin, C., Bienfait, G. and Lapointe, R. (2003) Heat flow in the western Superior Province of the Canadian shield, *Geophys. Res. Lett.*, **30** (12), 1637.

Rondenay, S., Bostock, M.G., Hearn, T.M., White, D.J. and Ellis, R.M. (2000) Lithospheric assembly and modification of the SE Canadian Shield: Abitibi–Grenville teleseismic experiment, *J. Geophys. Res.*, **105**(B6), 13735–13754.

Rychert, C.A., Rondenay, S. and Fischer, K.M. (2007) P–to–S and S–to–P imaging of a sharp lithosphere–asthenosphere boundary beneath eastern North America, *J. Geophys. Res.*, **112**, B08314.

Silver, P.G. and Chan, W.W. (1988) Implications for continental structure and evolution from seismic anisotropy, *Nature*, **335** (1 September).

Sol, S., Thomson, C. J., Kendall, J–M., White, D., VanDecar, J. C. and Asudeh, I. (2002) Seismic tomographic images of the cratonic upper mantle beneath the Western Superior Province of the Canadian Shield – a remnant Archean slab?, *Phys. Earth Planet. Int.*, **134**, 53–69.

Snyder, D. and Bruneton, M. (2007) Seismic anisotropy of the Slave craton, NW Canada, from joint interpretation of SKS and Rayleigh waves, *Geophys. J. Int.*, **168**.

Thompson, D., Helffrich, G., Bastow, I., Kendall, J–M., Wookey, J., Eaton, D. & Snyder, D. (2008) Mantle discontinuities beneath Hudson Bay, *Conference Abstract*, AGU Fall Meeting, San Francisco, USA.

Thompson, P. H., Judge, A. S. and Lewis, T. J. (1996) Thermal evolution of the lithosphere in the central Slave Province: Implications for diamond genesis, in *Searching for diamonds in Canada*, eds. LeCheminant, A. N. et al., Geological Survey of Canada Open File Report 3228, 151–160.

van der Lee, S. and Nolet, G. (1997) Upper mantle S velocity structure of North America, *J. Geophys. Res.*, **102**(10), 22815–22838.

Wessel, P. and Smith, W.H.F. (1995) New version of the Generic Mapping Tools released, *EOS Trans. AGU*, **76**, 329.

White, D.J., Helmstaedt, H., Harrap, R. and Thurston, P. (1998) The ori-

gin of our continent: LITHOPROBE seismic investigations in the Western Superior Transect, *CIM Bulletin*, **90**, 78–82.

White, D. J., Musacchio, G., Helmstaedt, H.H., Harrap, R.M., Thurston, P.C., van der Velden, A. and Hall, K. (2003) Images of a lower–crustal oceanic slab: Direct evidence for a tectonic accretion in the Archean western Superior province, *Geology*, **31** (11), 997–1000.

Wilson, D., Aster, R. & the RISTRA Group (2003) Imaging crust and upper mantle seismic structure in the southwestern United States using teleseismic receiver functions, *The Leading Edge*, **22**, 232–237.

Wilson, D. and Aster, R. (2005) Seismic imaging of the crust and upper mantle using regularized joint receiver functions, frequency–wave number filtering, and multimode Kirchhoff migration, *J. Geophys. Res.*, **110**, B05305.

Wilson, D. C., Angus, D. A., Ni, J. F. and Grand, S. P. (2006) Constraints on the interpretation of S–to–P receiver functions, *Geophys. J. Int.*, **165**, 969–980.

Young, R. A., Wright, J. and West, G. F. (1986) Seismic crustal structure northwest of Thunder Bay, in *Reflection Seismology: The Continental Crust, Geodyn. Ser.*, **14**, eds. Barazangi, M. and Brown, L., AGU, Washington, DC, 143–155.

Yuan, X., Kind, R., Li, X. and Wang, R. (2006) The S receiver functions: synthetics and data example, *Geophys. J. Int.*, **165** (2), 555–564.

Zeng, F. and Calvert, A.J. (2006) Imaging the upper part of the Red Lake greenstone belt, northwestern Ontario, with 3–D traveltime tomography, *Can. J. Earth Sci.*, **43**, 849–863.

Zhu, L. and Kanamori, H. (2000) Moho depth variation in southern California from teleseismic receiver functions, *J. Geophys. Res.*, **105**, 2969–2980.

Table and Figure Captions

Table 1. List of TWiST and FedNor stations showing latitude, longitude, number of P– and S–wave receiver functions, network, V_P/V_S ratio and depth H to Moho. The values in brackets represent the number of reprocessed ETDF P–wave receiver functions (see text for detials).

Figure 1. Map of the Western Superior Province showing the locations of the various experiments of the WST. Black triangles and inverted grey triangles are the TWiST and FedNor seismic stations, respectively; the N–S and E–W trending grey line represents the approximate location of the RWAR controlled seismic source lines; the grey circles represent the MT surveys; and the grey diamonds represent the heat flow measurements.

Figure 2. Global distribution of the events used in the P– and S–wave receiver function study. The 85 events for the P–receiver functions are shown as grey circles and the 50 events for the S–receiver functions are shown as black circles. Contours are shown for every 30° from the centre of the TWiST array.

Figure 3. CCP image sections for the Ps (top), PpPs (second from top) and PpSs (second from bottom) converted phases. Positive amplitudes (red) indicate a positive seismic impedance change moving downward. Each single converted phase CCP image shows a Moho signal at approximately 42 km depth as well as intra–crustal conversions. Also visible are sub–crustal signals at approximately 65 km (positive) and 55 km (negative) depth. There is potentially another discontinuity imaged at approximately 80 km, but it should be noted that at greater depths potential artifacts due the low data coverage

on the CCP imaging may be present. The ray coverage for the P–receiver function analysis is shown at the bottom right.

Figure 4. Combined P–receiver function image of the Ps, PpPs and PpSs converted phases (top) and interpreted section (bottom). The dashed lines are the inferred seismic discontinuities for the crust and upper mantle. The dashed–dotted lines indicate possible structure and the question mark symbol serves to indicate that it is not clear whether this structure ends abruptly or may actually dip towards the positive discontinuity at 65 km depth. The regions denoted by LVZ represent possible low–velocity zones. Below the inferred seismic discontinuity at approximately 65 km depth, there appears to be observable vertical and lateral heterogeneity around 80 km depth. However, this region may be affected strongly by artifacts, such as sub–crustal multiples (CM) and/or noisy P–receiver functions.

Figure 5. CCP image sections for the Sp converted phases. Negative amplitudes (red) indicate a positive seismic impedance change moving downward. The CCP images are for events with epicentral distances within 60°–75° (top), 57.5°–77.5° (second from top) and 55°–80° (second from bottom). The bottom panel shows the ray coverage for the S–receiver function CCP image for eventsbetween 55°–80°. The images are noticeably smoother than the P–receiver function images because the S–to–P converted phases are lower in frequency content.

Figure 6. Combined P– and S–receiver function image of the Ps, PpPs and PpSs and Sp converted phases (top) and interpreted section (bottom). The dashed lines are the inferred seismic discontinuities for the crust and upper

mantle, and the regions denoted by LVZ represent the low–velocity zones. The symbols 'G' highlight regions of velocity gradients observed by Musacchio et al. (2004) and in the CCP image coincide with weak (if any) crustal and sub–crustral discontinuities. The dashed–dotted lines indicate possible structure and the question mark symbol serves to indicate whether this structure ends abruptly or may actually dip towards the positive discontinuity at 65 km depth. The plus symbols indicate the H–κ stack estimates of the Moho depth below each station.

Figure 7. H–κ contour plot for FedNor station MUMO. The red dot shows the best result with associated 2 σ errors (95% confidence interval).

Figure 8. (Top) Raw P–wave receiver function plot with respect to epicentral distance for FedNor station MUMO. The lines indicate the predicted arrivals of the Ps, PpPs, and PsPs and PpSs phases assuming an average crustal P–wave velocity of 6.5 km/s, V_P/V_S ratio of 1.71 and crustal thickness of 39.2 km. (Bottom) Stacked receiver function for station MUMO. The middle line represents the jackknife mean and the two outer lines the 2 σ errors. The red and blue peaks highlight receiver function signal with at least 95% confidence in positive and negative conversions, respectively.

Figure 9. Top: Sketch summarising the results of the previous geophysical studies (see section 2). Bottom: Sketch summarising the results of the combined P– and S–receiver function analysis. To the right of both panels is the shear–wave velocity model of Kendall et al. (2002), where the grey region indicates the range of acceptable solutions of the surface–wave inversion from Kendall et al. (2002).

Receiver functions

Station	Latitude (°)	Longitude (°)	P–wave	S–wave	Network	V_P/V_S	H (km)
5010	48.317	-90.714	13(26)	5	TWiST	1.68 ± 0.04	46.7 ± 1.3
5030	48.662	-90.829	11(18)	0	TWiST	1.74 ± 0.02	45.8 ± 0.7
ATKO	48.823	-91.601	25(28)	1	FedNor	1.74 ± 0.02	43.7 ± 0.8
5050	49.003	-90.759	11(11)	5	TWiST	1.65 ± 0.12	46.9 ± 3.0
LDIO	49.175	-89.596	13(19)	1	FedNor	1.78 ± 0.02	43.8 ± 0.7
5070	49.340	-90.470	13(18)	6	TWiST	1.73 ± 0.03	43.6 ± 0.9
5090	49.665	-90.334	13(20)	5	TWiST	1.75 ± 0.02	46.0 ± 0.8
5110	50.017	-90.587	9(11)	5	TWiST	1.73 ± 0.02	42.6 ± 0.7
5130	50.359	-90.674	13(13)	5	TWiST	1.78 ± 0.02	40.1 ± 0.7
5150	50.695	-90.555	9(13)	3	TWiST	1.74 ± 0.03	39.7 ± 1.0
5170	51.032	-90.351	13(10)	0	TWiST	1.75 ± 0.04	41.7 ± 0.9
5190	51.353	-90.222	8(11)	6	TWiST	1.78 ± 0.05	39.1 ± 0.8
PKLO	51.499	-90.352	19(22)	5	FedNor	1.77 ± 0.03	39.0 ± 0.6
B11	51.647	-89.908	19(9)	5	TWiST	1.66 ± 0.03	42.2 ± 1.5
B12	52.050	-90.016	18(16)	4	TWiST	1.79 ± 0.02	39.2 ± 0.6
B13	52.411	-90.508	16(17)	9	TWiST	1.75 ± 0.03	38.3 ± 0.9
B14	52.568	-90.444	10(13)	4	TWiST	1.74 ± 0.03	38.9 ± 0.8
MUMO	52.613	-90.391	30(30)	6	FedNor	1.71 ± 0.04	39.2 ± 0.7
BBT	53.843	-89.878	24(0)	4	TWiST	1.72 ± 0.05	39.0 ± 1.0
BPW	54.988	-85.453	22(0)	9	TWiST	1.72 ± 0.02	39.0 ± 0.7
BFS	55.987	-87.652	7(0)	0	TWiST	1.77 ± 0.04	40.9 ± 1.5
		Total	316(351)	88	Average	1.74	41.7

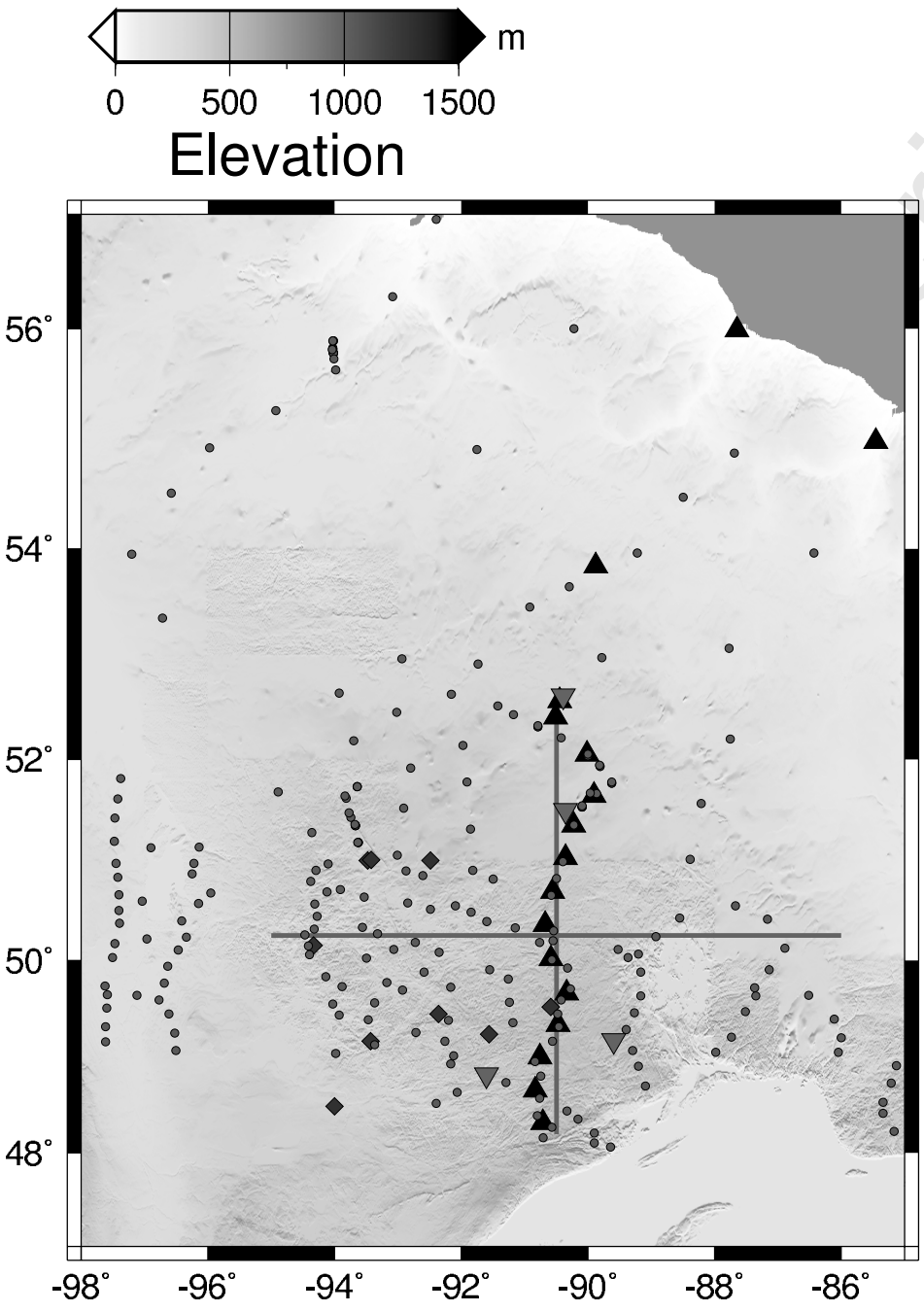

Fig. 1. Figure.

Fig. 2. Figure.

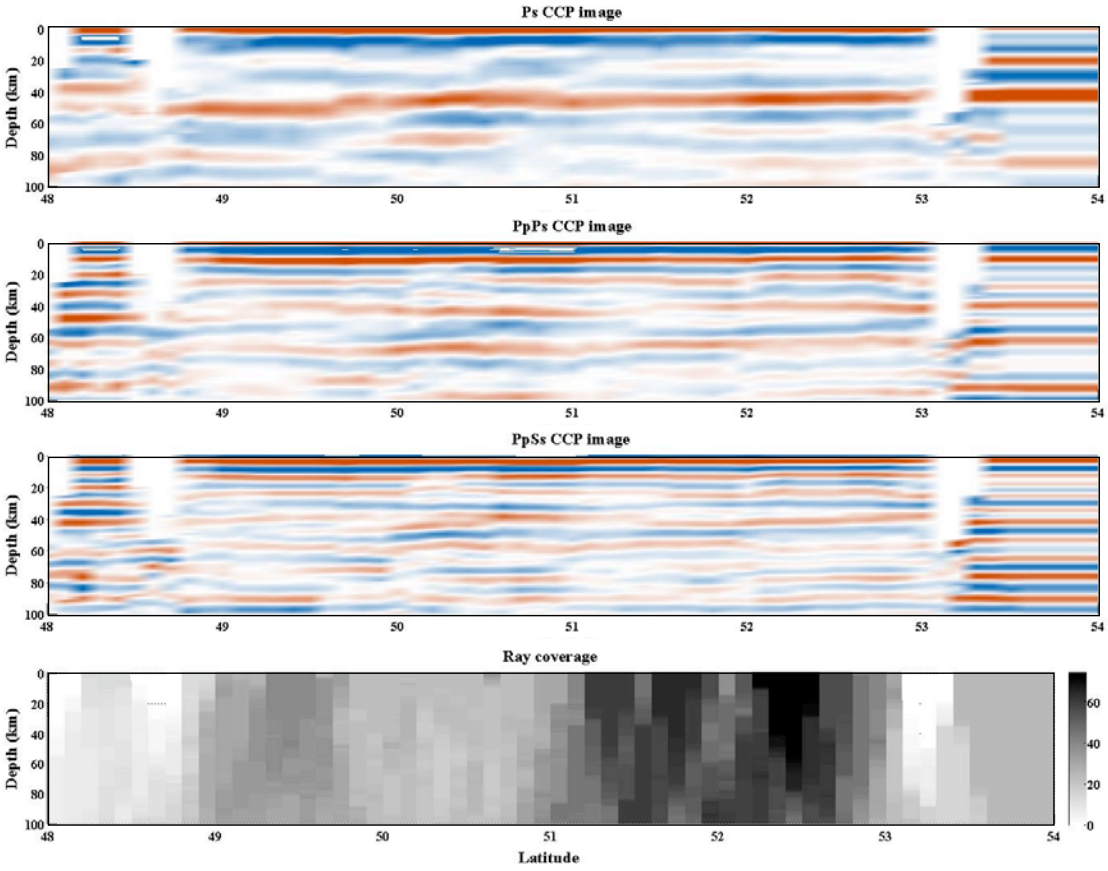

Fig. 3. Figure.

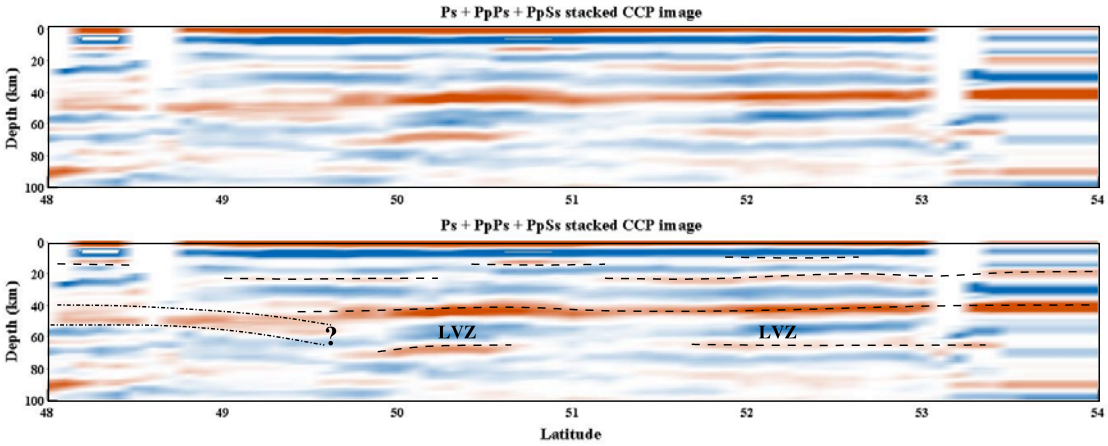

Fig. 4. Figure.

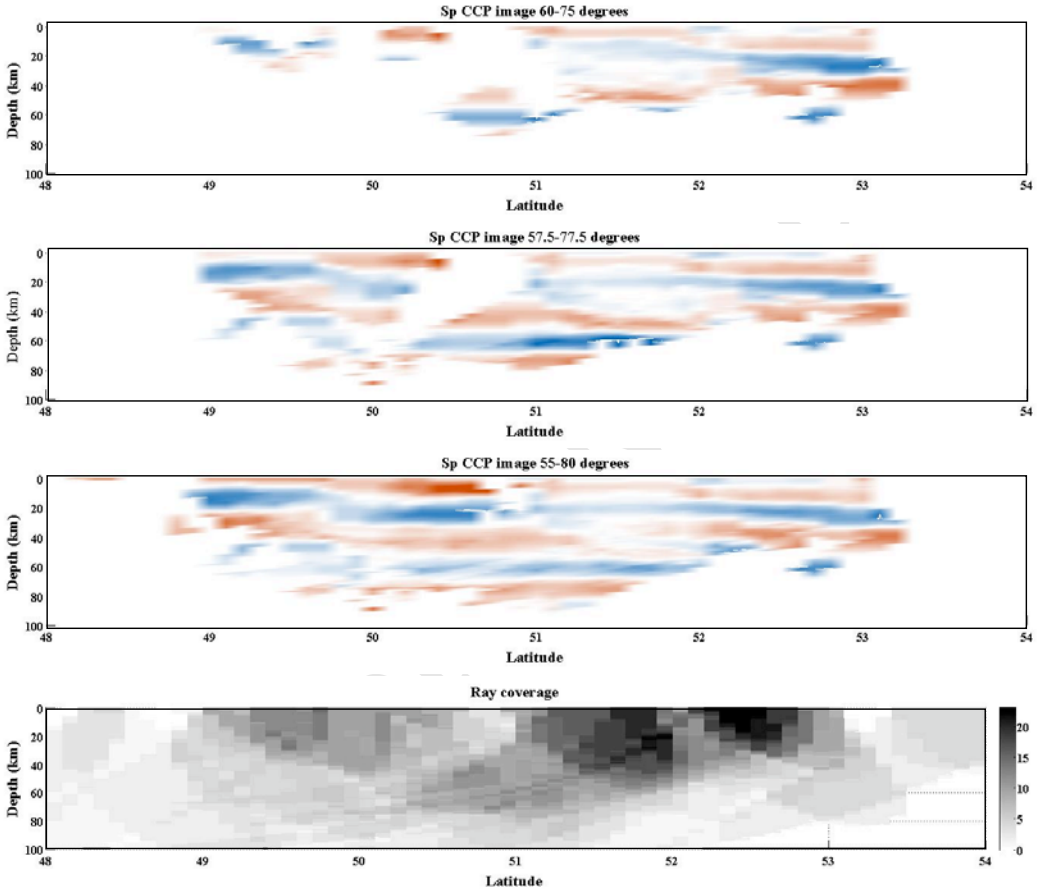

Fig. 5. Figure.

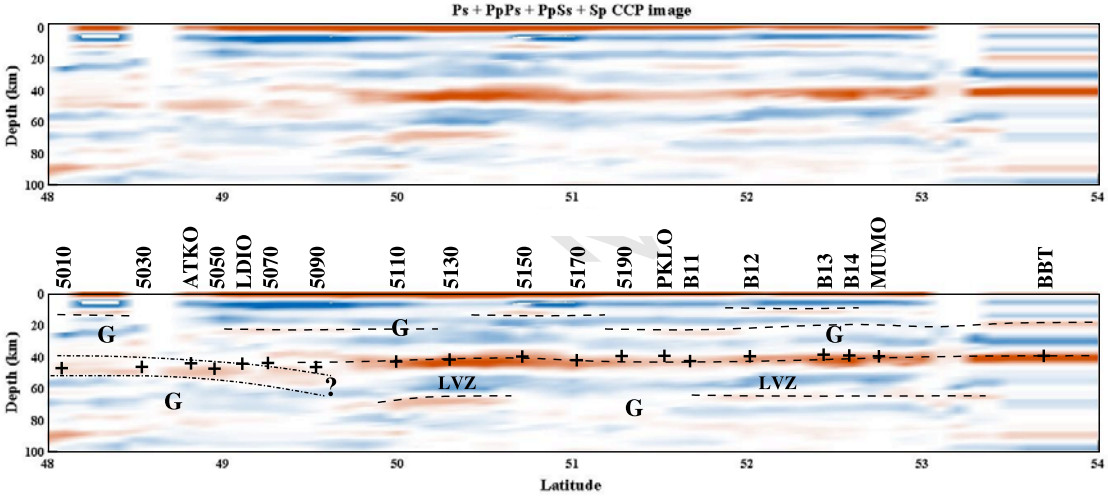

Fig. 6. Figure.

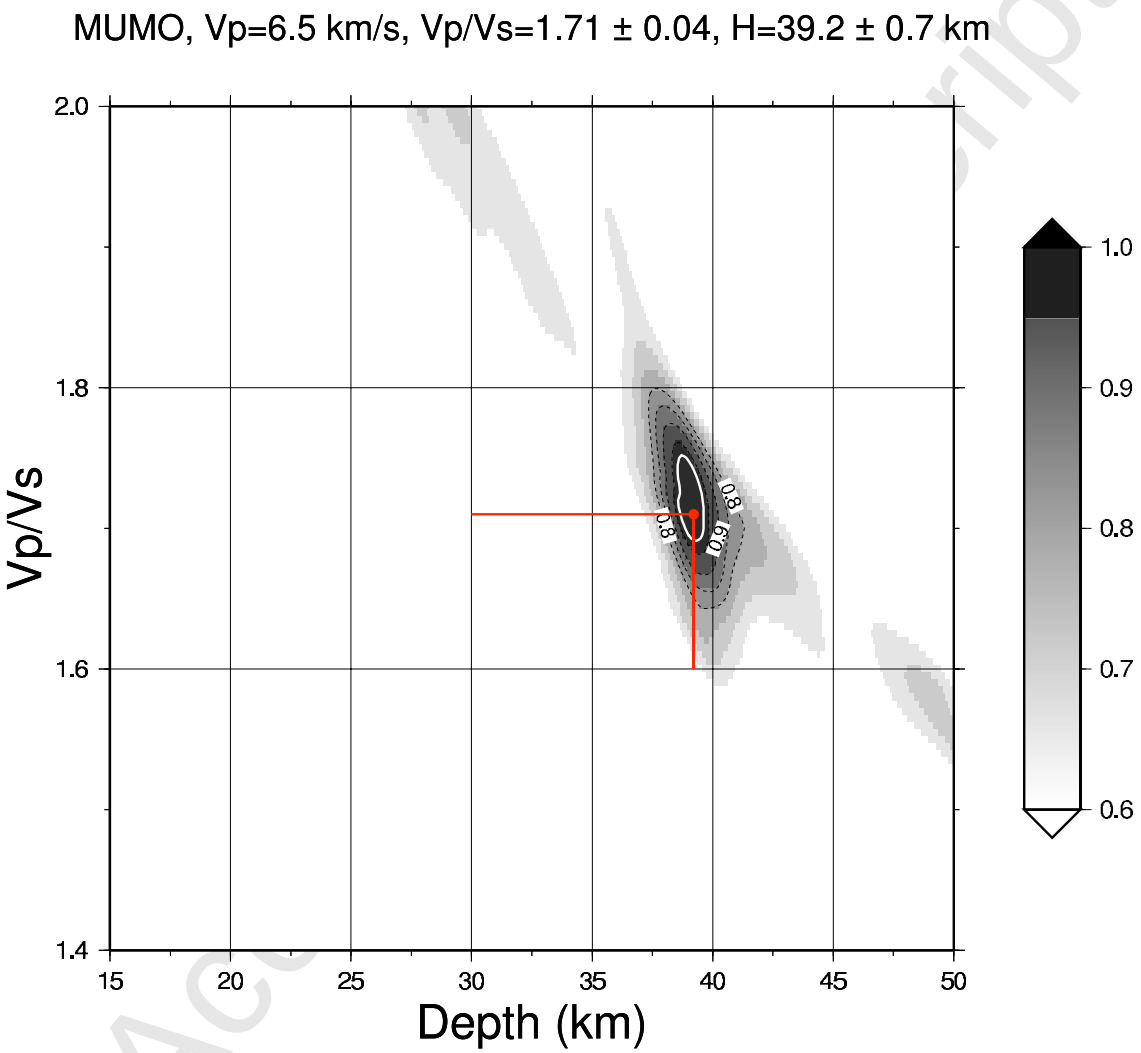

Fig. 7. Figure.

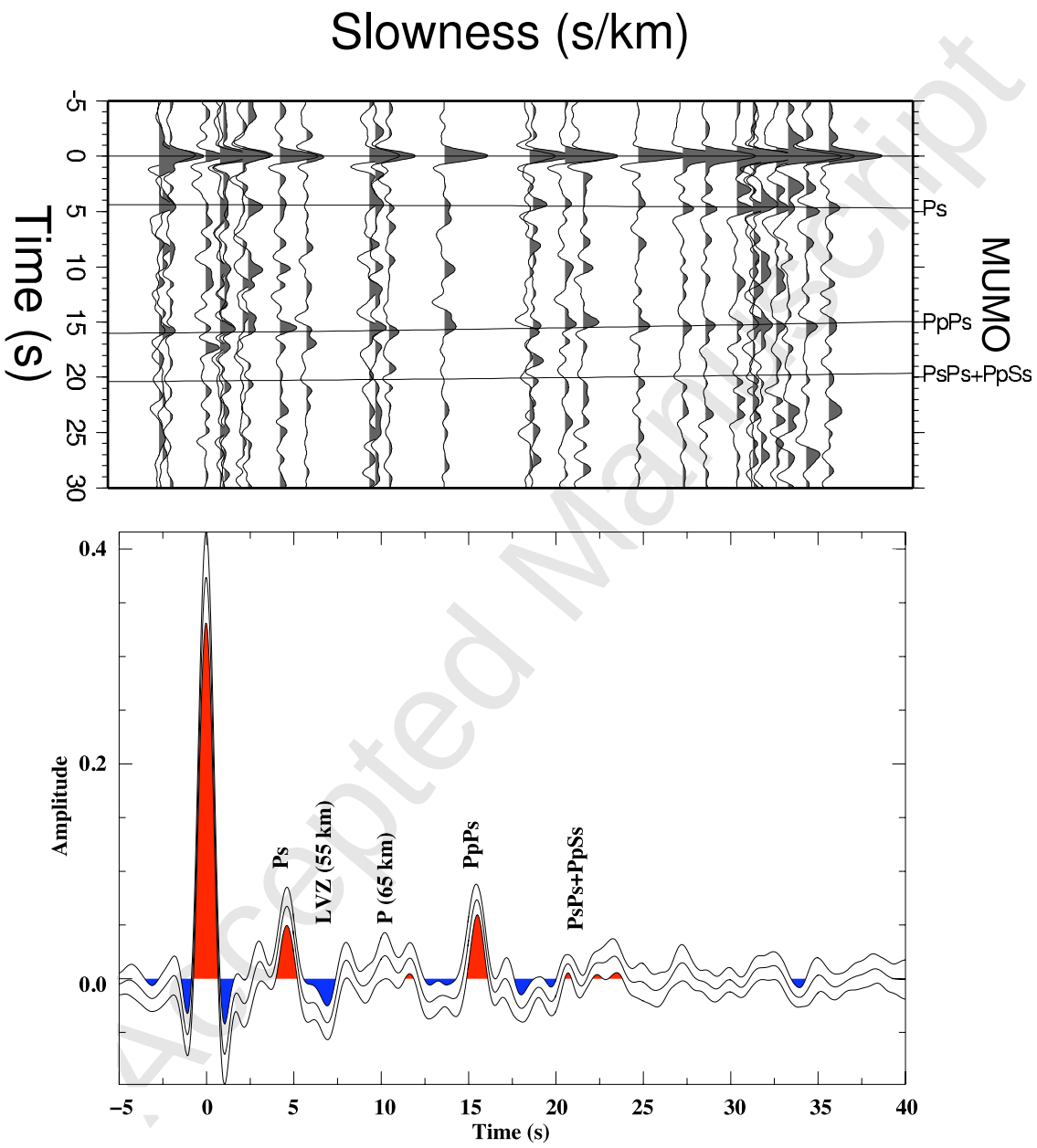

Fig. 8. Figure.

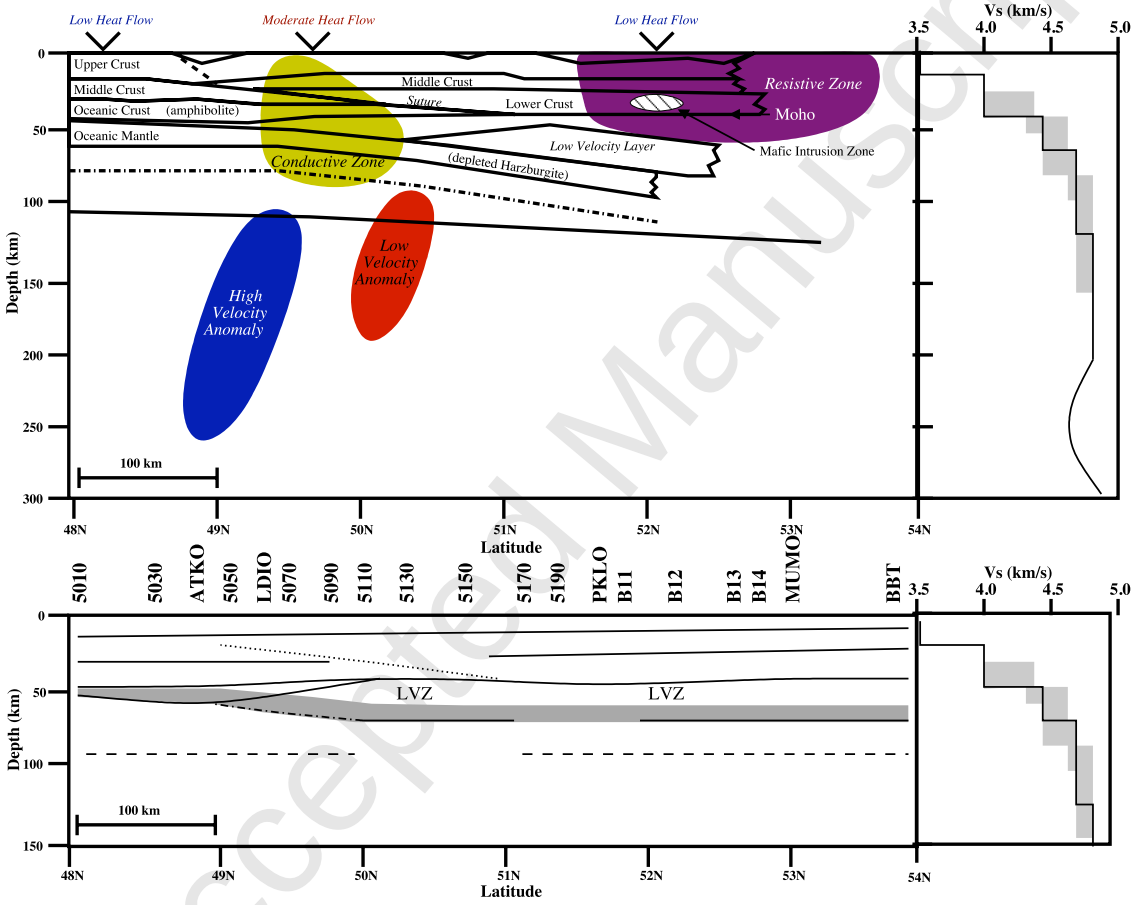

Fig. 9. Figure.